A Generative Adversarial Network-based Anomaly Detection in Japanese Paddy Fields using Sentinel-2

Ogawa S.[1] and Matsuoka M.[1*]

[1]Graduate School of Engineering, Mie University, 1577, Kurima-machiya, Tsu, Mie 514-8507, Japan

[*]matsuoka@info.mie-u.ac.jp

***Abstract*:** *Global warming and extreme weather events have caused a serious problem in rice growth. In addition, the decline in the number of farmers has led to the necessity of managing expansive tracts of farmland. Hence, it is important to quickly detect anomalies in agricultural fields for taking appropriate action. Satellite remote sensing has been used to determine the spatial distribution of crop growth in large agricultural fields. Mahalanobis distance (MD) and generative adversarial network (GAN) are often used as anomaly detection methods. Machine learning-based anomaly detection is currently utilized in the medical and manufacturing fields, thus there is a possibility of its utilizations in the field of remote sensing as well. The objective of this study is to detect anomalies in paddy fields over a wide area using satellite images based on generative adversarial network (GAN). We used the Multispectral Instrument (MSI) onboard Sentinel-2 observed on 17 July 2023, in the middle of the rice growing season. The target area was the entire Okayama Prefecture, Japan, and paddy field pixels were identified by farmland parcel polygon data. The considerable outliers, represented by clouds, were removed manually. To distinguish anomaly, the Mahalanobis' distance (MD) was calculated for each pixel using 10 bands with the spatial resolution of 10 m and 20 m. Anomalous pixels were determined based on the threshold for MD. We modified the GAN models from image-based to spectral-based architecture. Two models, the Fast Anomaly Detection with Generative Adversarial Networks (f-AnoGAN) and Efficient-GAN, were used to compare performance. Both models could generate similar spectral reflectance for normal paddy field pixels using the fully connected neural network, and could detect the anomalous pixels that have different spectra from those normal pixels. The ROC-AUC of anomaly detection was 95.5% for f-AnoGAN and 97.1% for Efficient-GAN, indicating the effectiveness of GAN. The problem is that we do not know whether a pixel is abnormal or not from an agricultural point of view, since it is divided into normal and abnormal pixels according to its numerical value.*

Keywords: Anomaly detection, generative adversarial network (GAN), Mahalanobis distance (MD), paddy field, Sentinel-2

INTRODUCTION

Background

In Japan, there have been numerous reports of quality losses in paddy rice due to high temperature (Ministry of Agriculture, Forestry and Fisheries, 2024). Thus, crops such as paddy rice are particularly sensitive to the climate change. In addition, the decline in the number of farmers has led to the necessity of managing expansive tracts of farmland. The area of farmland per management entity is increasing, and also the amount of abandoned farmland is increasing due to the aging of the farming population and lack of labor (Ministry of Agriculture, Forestry and Fisheries, 2024). Therefore, it is important to quickly detect anomalies in agricultural fields for taking appropriate actions. Satellite remote sensing has been used to determine the spatial distribution of crop growth in large agricultural fields. It makes easier to implement pesticide/fertilizer sprays and harvests at the appropriate time. Furthermore, Sentinel and Landsat satellite imagery is open data, so anyone can easily analyze the data.

Machine learning-based anomaly detection is expected to improve agricultural production by detecting the influences of pests and diseases at an early stage. Mahalanobis Distance (MD) is a statistical measure for measuring the distance between points and distributions in multivariate data analysis. A generative adversarial network (GAN) is a generative model that can learn features from prepared data and generate pseudo data. GAN is used not only for image generation, but also for removing mosaics from images, audio generation, and super-resolution. MD and GAN are also often used for anomaly detection as “unsupervised learning,” in which features are learned without providing correct data. Currently, GANs are widely used in the field of remote sensing, but most of them deal with super-resolution. Machine learning-based anomaly detection is currently utilized in the medical and manufacturing fields, thus there is a possibility of its utilizations in the field of remote sensing as well.

Problem Statement

The problem is that farmers with large tracts of farmland have difficulty in quickly recognizing and dealing with anomalies in their farmland. In addition, there are few papers on anomaly detection in farmland using satellite remote sensing, and the technology has not yet been put to practical use.

Objective

Objective of this study is to detect anomalies in paddy fields based on GAN using satellite image. Paddy field pixels from satellite images were classified as normal or abnormal using

MD. We used Fast Anomaly Detection with Generative Adversarial Networks (f-AnoGAN), one of the generative models specialized for anomaly detection. This model was modified from an image-based to a spectral-based architecture. By using a fully connected neural network, the model is expected to generate similar spectral reflectance for normal paddy field pixels. We also used efficient-GAN to compare the accuracy and verify the validity of the classification by MD.

Literature Survey

Various studies have suggested that anomaly detection using MD and GAN is valuable. Panda et al. (2021) analyzed hyperspectral images using Euclidean and Mahalanobis distances to classify neutrophils from Chronic Myeloid Leukemia (CML) versus healthy blood samples. Seven high information containing bands out of 61 or 49 bands were identified for each hyperspectral image using principal component analysis (PCA). The limitations of Euclidean distance in classification were described, including the need to represent a given distribution by a single point, since Euclidean distance is calculated between two points. As a result, The Euclidean distance was found to be superior when it came to sensitivity in detecting CML neutrophils whereas the Mahalanobis distance was better at detecting healthy neutrophils and distinguishing CML neutrophils from healthy neutrophils.

Schlegl et al. (2019) used f-AnoGAN to detect anomalies in retinal optical coherence tomography (OCT) images. They built a generative model of healthy training data, and proposed and evaluated a fast mapping technique of new data to the GAN's latent space. A discriminator guided image-to-image mapping approach (izif) was utilized for the first time for learning the mapping from images to latent encodings in a subsequent training step. As a result, the accuracy of anomaly detection using f-AnoGAN was 93%, which was higher than that of other methods. In addition, a visual Turing test with two retina experts showed that the generated images are indistinguishable from real normal retinal OCT images.

Wang et al. (2023) proposed a hyperspectral anomaly detection network based on variational background inference and generative adversarial framework (VBIGAN-AD). The proposed VBIGAN model could learn the background distribution characteristics of Hyperspectral Images and enhance the detection performance by the use of reconstruction errors. The VBIGAN framework consisted of sample and latent GANs, which establishes the relationship between data samples and latent samples through two sub-networks to capture the data distribution. The encoder, generator and the two discriminators each had a fully connected layer, and allowed for the generation and identification of pseudo-spectra. Experimental

results on five hyperspectral image datasets showed that the accuracy of the proposed model was higher than that of other methods.

Fujioka et al. (2020) used Efficient-GAN-based anomaly detection diagnose images of normal tissue, benign masses, or malignant masses on breast ultrasound. Their models are based on developed bidirectional GAN methods and simultaneously learn an encoder that maps input samples to a latent space along with a generator and discriminator during training. This avoided the computationally expensive step of recovering latent expressions during testing. The anomaly colormap was created by deriving the difference between the input test image and the image generated from the trained generator and by converting from grayscale to color scale (jet). Malignant masses had significantly higher anomaly scores than benign masses, and benign masses had significantly higher scores than normal tissues. The sensitivity, specificity, and the ROC-AUC for distinguishing normal tissue from benign and malignant masses were high, and the values for distinguishing normal tissue from malignant masses were even higher.

METHODOLOGY

Satellite Data

Multispectral Instrument (MSI) onboard Sentinel-2 was used for satellite images because they have higher spatial and temporal (5 days) resolutions than other mid-spatial resolution images. The MSI specifications are shown in Table 1. The target area is Okayama Prefecture, Japan where there is relatively little variation in cropping season. The observation date is 17 July 2023, in the middle of the rice growing season. The data were downloaded via The Copernicus Data Space Ecosystem, considering the geographic locations, season, and cloud coverage. Sentinel-2 has 13 bands, but we used 10 bands with spatial resolutions of 10 and 20 m (Sentinel Wiki 2024). In other words, three bands in the visible region, three bands in the red-edge region, two bands in the near-infrared region, and two bands in the short wavelength region were used.

Table 1: MSI Specifications

Sentinel-2	
Satellite Platform	Sentinel-2B
Equipments	Multispectral Instrument (MSI)
Product type	Level 1C
Observation width (km)	290

Observation frequency (day)		10	
Spectral wave region (nm) and spatial resolution (m) of the band used in this study	Band 2, Blue	490	10
	Band 3, Green	560	10
	Band 4, Red	665	10
	Band 5, VNIR	705	20
	Band 6, VNIR	740	20
	Band 7, VNIR	783	20
	Band 8, NIR	842	10
	Band 8a, NIR	865	20
	Band 11, SWIR	1610	20
	Band 12, SWIR	2190	20

Paddy Field Map

Farmland parcel polygon data was used to identify the location of paddy fields. This polygon data, called "fude polygon" in Japanese, is information on agricultural land parcels that can be used in geographic information system (GIS) software. The data have been developed by the Statistics Department of the Ministry of Agriculture, Forestry and Fisheries (MAFF) in Japan for a comprehensive survey of arable land area. Each polygon has attribute data of an ID, type of arable land, year of publication, and latitude and longitude center-of-gravity coordinates. The data were downloaded for the fiscal year 2023 from the MAFF site. Only rice fields were used between two types of arable land (fields and paddies of rice).

Image Processing

The considerable outliers, mainly due to clouds, were removed manually. In addition, all bands with a spatial resolution of 20 m were interpolated to 10 m. The polygon data divided by city/town/village is united into one. The polygons as vector data were shrunk boundaries in order that all the Sentinel-2 pixels contain only the paddy field. Figure 1 shows the 10m-resolution Sentinel-2 pixels of paddy field selected by the parcel polygon data. It can be seen that the paddy fields are color-coded according to the ID values assigned to them. These processes were performed by QGIS, an open-source software with geospatial information data viewing, editing, and analysis capabilities.

Figure 1: Paddy Field Pixels in Sentinel-2 Colored by Polygon ID

For machine learning, the 10-band images were overlaid, and the coordinates of each paddy pixel were identified by its assigned ID and reflectance was extracted. The IDs, coordinates, and reflectance of all 890314 extracted pixels were saved in a CSV file.

Mahalanobis Distance (MD)

MD (De Maesschalck, R., 2000) is one of the anomaly detection methods for unsupervised learning. It is a distance measure in multivariate space, where the correlation of each dimension can be expressed as a distance. Unlike Euclidean distance, it is computed using the inverse of the variance-covariance matrix of the data set of interest, thus taking into account correlations in the data. Therefore, the degree of outliers from the distribution can be quantified. However, when the investigated data are measured over a large number of variables, they can contain much redundant or correlated information. This so-called multicollinearity in the data leads to a singular or nearly singular variance–covariance matrix that cannot be inverted. In addition, the number of objects in the data set must be greater than the number of variables. In this study, no dimensionality reduction was performed because the number of pixels is 890314 and the number of bands is 10. The formula for calculating MD is expressed as follows:

$$d = \sqrt{(\vec{x} - \vec{\mu})^{\mathrm{T}} \Sigma^{-1} (\vec{x} - \vec{\mu})},$$

where $\vec{x}$ is vector of paddy field pixel with 10 bands, $\vec{\mu}$ is the mean vector of $\vec{x}$, Σ is variance-covariance matrix of size 10×10.

The MD calculated for all 890314 pixels extracted from the satellite image is shown in Figure

2. More than 90% of the pixels have MDs less than five, and the value is larger when the pixel is an abnormal pixel.

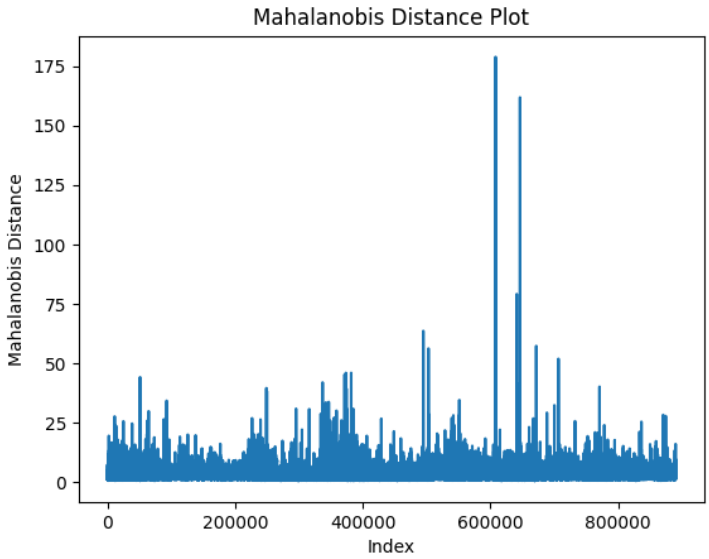

Figure 2: Mahalanobis Distances

Dataset

We set a threshold value of 10.0 for the MD to divide the pixels into normal and abnormal pixels. Table 2 shows the datasets used for this study. The training data consisted of 100000 data for normal pixels only. The test data consists of 4000 normal pixels and 4002 abnormal pixels. The 782312 pixels not included in the dataset were not used for training. ID value overlap between training and test data was not taken into account. The pixel values for each band were normalized to zero to one. The shape of input data is 1×10, corresponding pixel by band, respectively.

Table 2: Dataset

train	test	
normal	normal	abnormal
100000	4000	4002

To confirm the difference of normal and anomolous data, average spectral reflectance was calculated. Figure 3(a) shows the average reflectance calculated from 100,000 normal pixels used for training, and Figure 3(b) is average reflectance of 4002 anomalous pixels used for testing. Although the general shape of both graphs is similar, it can be seen that the reflectance values of anomalous pixels are generally larger. In particular, the values in bands 6, 7, 8, 8a, 11, and 12 are larger than 0.1.

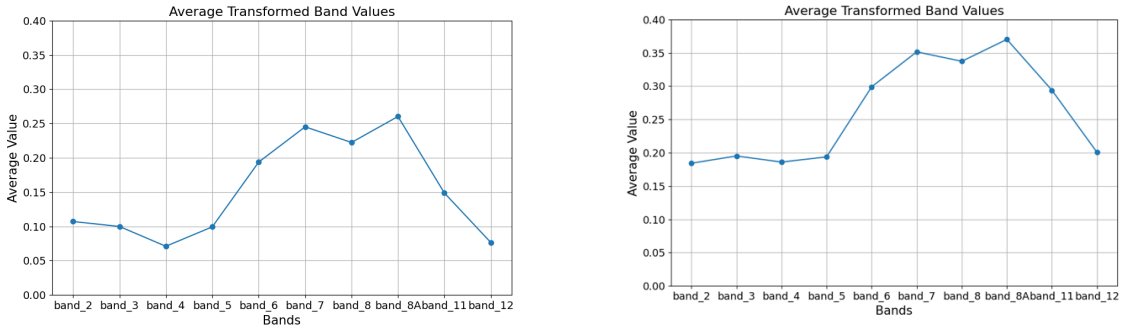

(a) Normal spectrum (b) Abnormal spectrum

Figure 3: Average of the Spectrum

Fast Anomaly Detection with Anomaly Detection (f-AnoGAN)

The f-AnoGAN is one of the anomaly detection models and consists of three parts: a generator, a discriminator, and an encoder. The f-AnoGAN is an improvement on AnoGAN (Schlegl, T., 2017), which is time consuming due to the presence of a learning phase during inference. In f-AnoGAN, the search by gradient descent during the inference phase is eliminated to speed up the inference process. The WGAN architecture is usually used in f-AnoGAN. Following the training for the generator and the discriminator using only normal pixels, the encoder is trained with optimized parameters of the generator and the discriminator. The WGAN uses the Wasserstein distance, a method to measure the distance between two probability distributions, as a loss function. The learning optimization was achieved by applying a gradient penalty to the loss function. The encoder training used a residual-aware izi_f architecture of the feature space populated by the discriminator, which is a reliable basis for identifying anomalous images. In addition to the same data used for WGAN training, i.e., trained using only normal images, image statistics for real and reconstructed images were further computed. The loss function for the izi_f encoder training is as follows:

$$L_{izi_f}(x) = \frac{1}{n} \cdot \| x - G(E(x)) \|^2 + \frac{k}{n_d} \cdot \| f(x) - f\left(G(E(x))\right) \|^2,$$

where x is input image, $G(E(x))$ is reconstructed image, $\| \cdot \|^2$ is sum of squared residuals, n is the number of pixels in an image, $f(\cdot)$ is Discriminator features of an intermediate layer, n_d is the dimensionality of the intermediate feature representation, k is weighting factor. The degree of anomaly is calculated by comparing the generated image with observed image using test dataset which contains both of normal and abnormal images.

The anomaly detection of f-AnoGAN determines the anomaly score for each test data. It is expressed by the following equation:

$$A(x) = A_R(x) + k \cdot A_D(x) ,$$

where x is test data, $A(x)$ is anomaly score $A_R(x)$ is mean squared error of real and fake spectrum, $A_D(x)$ is mean squared error of discriminating features between real and fake spectrum, k is weight coefficient.

We modified f-AnoGAN from image-based to spectral-based architecture. In the image-based model, feature extraction is performed by down-sampling with convolutional layers. In the spectral-based model, we used the fully connected layer to generate the similar spectral reflectance for normal paddy field pixels. In addition, dimensionality compression was performed by setting the number of dimensions of the latent space to 5 in the encoder training.

Efficient-GAN

Efficient-GAN (Zenati, H., 2018) is another popular GAN-based architecture for anomaly detection. It also consists of three parts: a generator, a discriminator and an encoder, same as f-AnoGAN. However, Efficient-GAN employs a bidirectional GAN called BiGAN (Donahue, J., 2017), which simultaneously learns an encoder that maps input samples to the latent space along with a generator and discriminator during training. This avoids the computationally expensive step of recovering latent representations during testing. The generator, discriminator, and encoder share the same loss function, and the model is updated so that the encoder and generator minimize, and the discriminator maximizes. The loss functions $min_{G,E}\ max_D V(D,E,G)$, with $V(D,E,G)$ defined as follows:

$$V(D,E,G) = \mathbb{E}_{x\sim p_X}\left[\mathbb{E}_{z\sim p_E(\cdot|x)}\left[\log D(x,z)\right]\right] + \mathbb{E}_{z\sim p_z}\left[\mathbb{E}_{x\sim p_G(\cdot|z)}\left[1 - \log D(x,z)\right]\right],$$

where $p_X(x)$ is the distribution over the data, $p_Z(z)$ is the distribution over the latent representation, $p_E(z|x)$ and $p_G(x|z)$ are the distribution induced by the encoder and generator respectively. An anomaly score is computed by the comparison between model-output image generated from input image and the input image itself. Then anomaly detection is carried out based on this anomaly score.

Efficient-GAN anomaly detection uses an anomaly score that measures how anomalous the test data is based on a convex combination of reconstruction loss and discriminator-based loss. The calculation formula is as follows:

$$A(x) = \alpha L_G(x) + (1-\alpha)L_D(x),$$

where x is test data, $A(x)$ is anomaly score $L_G(x)$ is a reconstruction loss, $L_D(x)$ is a discriminator-based loss, α is Random coefficient of $0 < \alpha < 1$.

Evaluation

The ROC-AUC, which is often used in the evaluation of classification problems, is used to evaluate the accuracy of anomaly detection. It represents the area under the ROC curve with the true positive rate on the vertical axis and the false positive rate on the horizontal axis. The ROC curve is represented by plotting the values of the true positive rate and the false positive rate for different threshold values for normal and abnormal classification. In addition, the optimal threshold value is found based on the ROC curve, the predicted labels are generated at that threshold value, and the confusion matrix is computed by comparing the predicted labels with the actual labels. Using each element of the confusion matrix, we used accuracy, fit rate, reproducibility, and F1-score, which is the harmonic mean of fit rate and reproducibility, as evaluation indices. Each evaluation index is calculated as follows:

$$Accuracy = \frac{TP + TN}{TP + FP + FN + TN},$$

$$Precision = \frac{TP}{TP + FP},$$

$$Recall = \frac{TP}{TP + FN},$$

$$F1 = \frac{2 \times (Precision \times Recall)}{Precision + Recall},$$

where TP is the number of abnormal pixels predicted as abnormal (True positive), FP is the number of normal pixels predicted as abnormal (False positive), FN is the number of abnormal pixels predicted as abnormal (False negative), TN is the number of normal pixels predicted as normal (True negative).

RESULTS AND DISCUSSION

Model Training

Two models were trained: f-AnoGAN and Efficient-GAN. All algorithms in this study were computed in Python 3.12.1 and the two GAN models were implemented using Pytorch, which is a machine learning library. The running environment was MacOS with an 8-core CPU.

(a) Training of f-AnoGAN

The WGAN was trained with an epoch of 300, batch size of 4000, and learning rate of 0.0002; the encoder was trained with an epoch of 100, batch size of 000, and learning rate of 0.0002. Figure 4(a) shows the loss scores of the generator and the discriminator in the WGAN training. Both of the two losses converged to zero, indicating that the learning was successful. Here, the loss score of the generator is less than zero, but this is usual that the loss

function in WGAN is less than zero. Figure 4 (b) shows the loss score of the encoder. The encoder was trained using the learned WGAN, and like the WGAN, the encoder's loss score converged to zero, indicating that it was successfully trained.

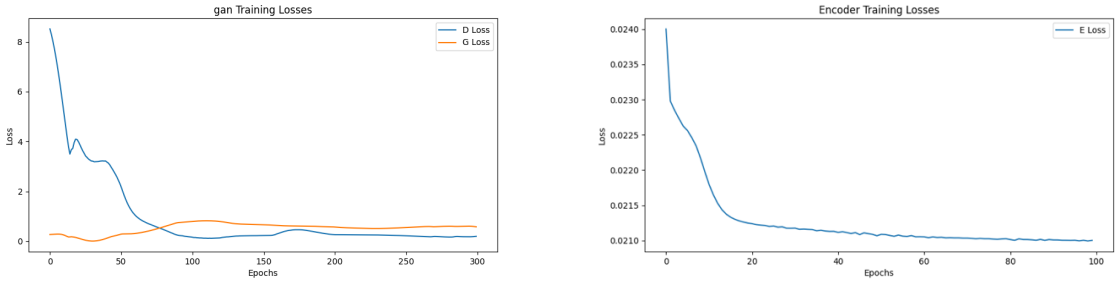

(a) Losses of generator and discriminator (b) Losses of encoder

Figure 4: Result of F-AnoGAN Training

(b) Training of Efficient-GAN

BiGAN training was trained with an epoch of 300, a batch size of 3000, and a learning rate of 0.0002. Figure 5 shows the loss scores of the generator, discriminator, and encoder in BiGAN training. encoder and generator are combined because they have the same loss function. Both loss scores are rising and falling, indicating that learning is unstable.

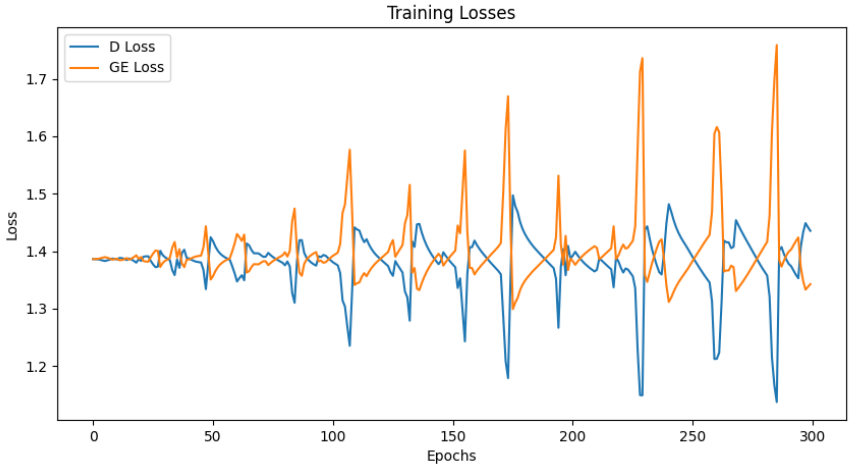

Figure 5: Result of BiGAN Training

Comparison of Spectral Reflectance

The average of the spectra generated in the final batch of training for each GAN was compared to the average of the normal spectral reflectance shown in Figure 3(a). Since a sigmoid function was used at the end of the generator model, the spectra were generated as if they were probability distributions. Figure 6(a) shows the distribution of the average of the spectra generated by WGAN. The higher values in bands 6, 7, 8, and 8a capture the characteristics of the normal spectrum shown in Figure 3(a). Figure 6(b) shows the

distribution of the average of the spectra reconstructed by the encoder. As in WGAN, the values in bands 6, 7, 8, and 8a are high. However, the values in bands 6, 7, and 8 are lower and the values in band 8a are reconstructed higher. Figure 6(c) shows the distribution of the average of the spectra generated by BiGAN. The values in Band 4 are very high, while those in Bands 6 and 8a are slightly lower.

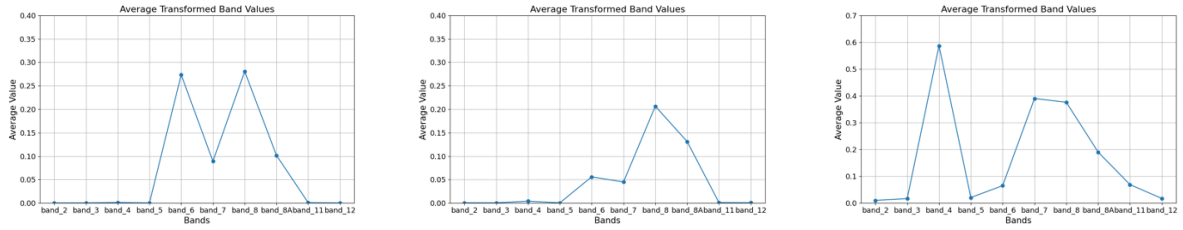

(a) Spectrum generated by WGAN (b) Spectrum reconstructed by the encoder (C) Spectrum generated by BiGAN

Figure 6: Comparison of Spectral Reflectance

Anomaly Detection

Figure 7(a) shows the distribution of anomaly scores for test data calculated by anomaly detection using f-AnoGAN. The vertical axis of the graph is in logarithmic scale for clarity. Anomaly scores range from approximately 0.001 to 1.3, indicating a clear separation between abnormal and normal. Figure 7(b) shows the ROC curve. The ROC-AUC score was as high as 0.954. Figure 7(c) shows a clear visualization of the confusion matrix. Normal pixels in the test data were often predicted to be abnormal. It is thought that this is because normal pixels near the MD threshold were predicted to be anomalous pixels.

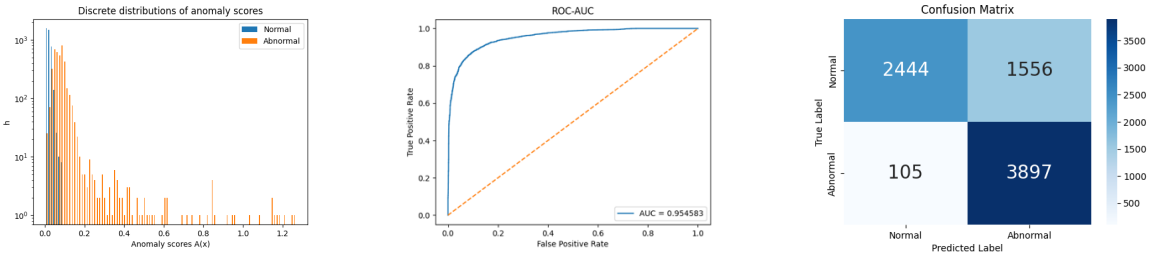

(a) distribution of anomaly scores (b) ROC curve (c) confusion matrix

Figure 7: Result of F-AnoGAN

Figure 8(a) shows the distribution of anomaly scores for test data calculated by anomaly detection using Efficient-GAN. The range of anomaly scores is approximately 1.0 to 4.5, indicating a clear separation between normal and abnormal. Figure 8(b) shows the ROC curve. The ROC-AUC score was 0.970, higher than f-AnoGAN. Figure 8(c) shows a clear

visualization of the confusion matrix. As with f-AnoGAN, normal pixels in the test data were often predicted as abnormal pixels.

Table 3 shows the values of Accuracy, Precision, Recall, and F-1 scores for f-AnoGAN and Efficient-GAN calculated from the confusion matrix. Both models have low Precision and high Recall. We can say that two models do not miss anomalous pixels.

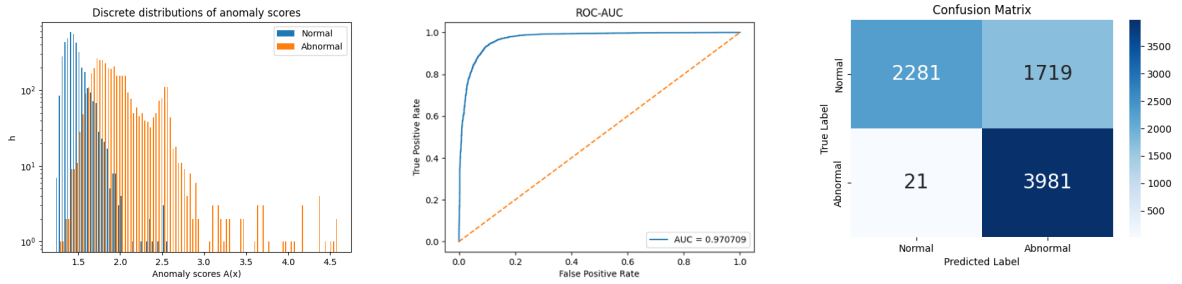

(a) distribution of anomaly scores

(b) ROC curve

(c) confusion matrix

Figure 8: Result of Efficient-GAN

Table 3: Evaluation

	Accuracy	Precision	Recall	F-1 score
f-AnoGAN	**0.792**	**0.715**	0.974	**0.824**
Efficient-GAN	0.783	0.698	**0.995**	0.821

Correlation between MD and Anomaly Score

We determined the correlation coefficients between the anomaly scores of the test data calculated by GAN and MD. Figure 9(a) shows the scatter plots of the anomaly scores calculated by f-AnoGAN and MD. The overall correlation coefficient was 0.633, indicating a correlation. However, when the correlation coefficient was narrowed down to only the abnormal pixels, the correlation coefficient was 0.490, which did not show much correlation. Figure 9(b) shows the scatter plot of anomaly scores calculated by Efficient-GAN and MD. The overall correlation coefficient was 0.682, indicating a correlation. However, it was also low for anomaly pixels, with a correlation coefficient of 0.339. Overall, MD and GAN results are positively correlated, with a reasonably high correlation coefficient. The separation of abnormal from normal in MD is the result of successful learning. Both scatter plots show upward and sideways extending distributions. GAN may detect anomalies from a different perspective than MD.

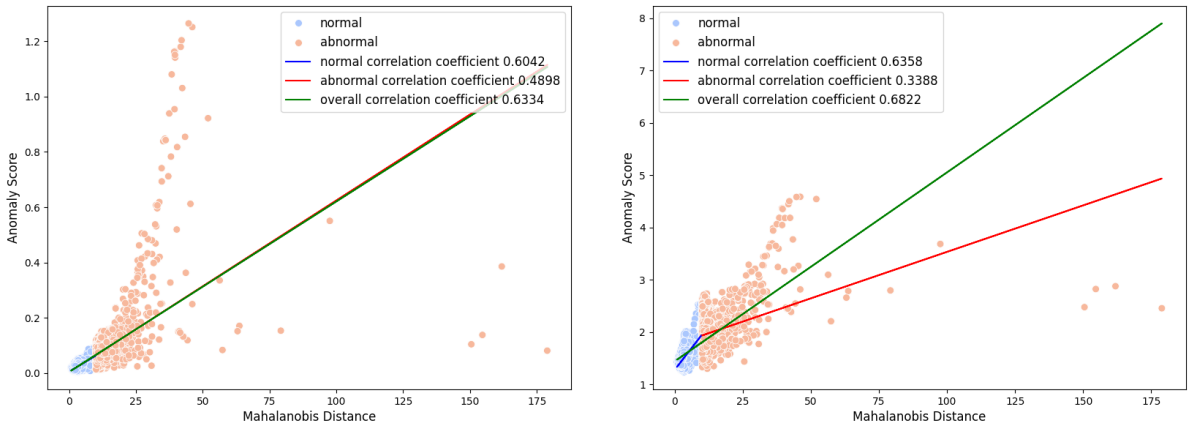

(a) f-AnoGAN (b) Efficient-GAN

Figure 9: Comparison of Correlation Coefficient

CONCLUSION

In this study, the anomaly detection by GAN was verified for the paddy field using satellite data. A GAN modified from an image-based to a spectral-based architecture was trained on data divided into normal and abnormal pixels according to MD thresholds. The realistic spectral reflectance could be generated using fully connected layer, and anomalous pixels could be detected by GAN. The ROC-AUC of anomaly detection was 95.5% for f-AnoGAN and 97.1% for Efficient-GAN, which was comparable to classification by MD. However, there was no significant correlation between anomaly scores and MD.

The main problem is that we do not know whether a pixel is abnormal or not, from an agricultural point of view, since it is divided into normal and abnormal pixels according to its numerical value. It is necessary to visually check the pixels that are determined to be abnormal. In the future, we intend to clarify what kind of problems are occurring in paddy fields according to the degree of anomaly.

References

De Maesschalck, R., Jouan-Rimbaud, D., & Massart, D.L. (2000). The Mahalanobis distance. Vol. 50, No. 1, pp. 1-18. *Chemometrics and Intelligent Laboratory Systems.* Elsevier. https://doi.org/10.1016/S0169-7439(99)00047-7

Donahue, J., Krähenbühl, P., & Darrell, T., (2017). Adversarial feature learning. *5th International Conference on Learning Representations* (ICLR), *24-26 April 2017*, *Touson, France*. https://doi.org/10.48550/arXiv.1605.09782

Fujioka, T., Kubota, K., Mori, M., Kikuchi, Y., Katsuta, L., Kimura, M., Yamaga, E., Adachi, M., Oda, G., Nakagawa, T., Kitazume, Y., & Tateishi, U. (2020). Efficient anomaly detection with generative adversarial network for breast ultrasound imaging. *Diagnostics.* Vol. 10, No. 7, pp. 456. https://doi.org/10.3390/diagnostics10070456

Ministry of Agriculture, Forestry and Fisheries. Impacts of Climate Change on Paddy Rice. Retrieved September 7, 2024, from https://www.maff.go.jp/j/seisan/kankyo/ondanka/attach/pdf/index-133.pdf

Ministry of Agriculture, Forestry and Fisheries. Statistics on Agricultural Land. Retrieved September 8, 2024, from https://www.maff.go.jp/j/tokei/sihyo/data/10.html

Panda, A., Pachori, R. B., & Sinnappah-Kang, N. D. (2021). Classification of chronic myeloid leukemia neutrophils by hyperspectral imaging using Euclidean and Mahalanobis distances. *Biomedical Signal Processing and Control.* Vol. 70. No. 103025. Elsevier. https://doi.org/10.1016/j.bspc.2021.103025

Schlegl, T., Seeböck, P., Waldstein, S. M., Schmidt-Erfurth, U., & Langs, G. (2017). Unsupervised anomaly detection with generative adversarial networks to guide marker discovery. *International conference on information processing in medical imaging,* pp. 146-157. Springer. https://doi.org/10.1007/978-3-319-59050-9_12

Schlegl, T., Seeböck, P., Waldstein, S. M., Langs, G., & Schmidt-Erfurth, U. (2019). f-AnoGAN: Fast unsupervised anomaly detection with generative adversarial networks. Vol. 54. *Medical Image Analysis.* Elsevier. https://doi.org/10.1016/j.media.2019.01.010

Sentinel Wiki. Sentinel-2. Retrieved September 9 ,2024, from https://sentiwiki.copernicus.eu/web/s2-mission

Wang, Z., Wang, X., Tan, K., Han, B., Ding, J., & Liu, Z. (2023). Hyperspectral anomaly detection based on variational background inference and generative adversarial network. Vol. 143. *Pattern Recognition*. Elsevier. https://doi.org/10.1016/j.patcog.2023.109795

Zenati, H., Foo, C. S., Lecouat, B., Manek, G., & Chandrasekhar, V. R. (2018). Efficient gan-based anomaly detection. arXiv preprint arXiv. https://doi.org/10.48550/arXiV.1802.06222